

Article

Open Access

Iterative projection meets sparsity regularization: towards practical single-shot quantitative phase imaging with in-line holography

Yunhui Gao¹  and Liangcai Cao^{1,*} 

Abstract

Holography provides access to the optical phase. The emerging compressive phase retrieval approach can achieve in-line holographic imaging beyond the information-theoretic limit or even from a single shot by exploring the signal priors. However, iterative projection methods based on physical knowledge of the wavefield suffer from poor imaging quality, whereas the regularization techniques sacrifice robustness for fidelity. In this work, we present a unified compressive phase retrieval framework for in-line holography that encapsulates the unique advantages of both physical constraints and sparsity priors. In particular, a constrained complex total variation (CCTV) regularizer is introduced that explores the well-known absorption and support constraints together with sparsity in the gradient domain, enabling practical high-quality in-line holographic imaging from a single intensity image. We developed efficient solvers based on the proximal gradient method for the non-smooth regularized inverse problem and the corresponding denoising subproblem. Theoretical analyses further guarantee the convergence of the algorithms with prespecified parameters, obviating the need for manual parameter tuning. As both simulated and optical experiments demonstrate, the proposed CCTV model can characterize complex natural scenes while utilizing physically tractable constraints for quality enhancement. This new compressive phase retrieval approach can be extended, with minor adjustments, to various imaging configurations, sparsifying operators, and physical knowledge. It may cast new light on both theoretical and empirical studies.

Keywords: Phase retrieval, Quantitative phase imaging, Compressive sensing, Digital holography

Introduction

The phase of an optical field contains various sources of information. Holography, invented by Gabor in 1947¹, provides access to phase information and has been used as a powerful imaging technique^{2,3}. At the optical frequency, however, electromagnetic waves oscillate so fast that the

detection devices can directly record only the average incident power. The loss of phase information poses unique challenges for the numerical inversion of the imaging process, leading to the so-called “twin-image” effect that severely degrades the imaging quality^{4,5}. As a result, phase retrieval, or the recovery of the phase from intensity-only measurements, remains a longstanding issue and lies at the heart of digital holography and many related optical imaging techniques⁶. In recent years, phase retrieval has

Correspondence: Liangcai Cao (clc@tsinghua.edu.cn)

¹State Key Laboratory of Precision Measurement Technology and Instruments, Department of Precision Instruments, Tsinghua University, Beijing 100084, China



regained increasing research interests following the development of computational imaging, which leverages advancements in signal processing theory, numerical algorithms, hardware design, and computation power⁷.

Existing phase retrieval methods for in-line holography can be broadly classified into two categories, namely diversity phase retrieval and compressive phase retrieval. The former approach requires taking multiple images with some data diversity that translate phase information into intensity distribution. This can be achieved, for example, by varying the imaging distance^{8–10}, illumination wavelength^{11–14}, probe position^{15–17}, illumination angle^{18–20}, and modulation pattern^{21–24}. While this approach can achieve quantitative phase imaging with increased data diversity and redundancy, it sacrifices the temporal resolution, system cost, and complexity. As an alternative, compressive phase retrieval takes a different path by exploring additional prior knowledge of the wavefield, which could potentially achieve phase recovery beyond the information-theoretic limit or even from a single shot.

Historically, early works tackled the phase ambiguity problem by utilizing simple yet effective physical constraints such as non-negativity^{25,26}, support^{27–29}, absorption³⁰, histogram³¹, and atomicity³². These constraints are typically enforced via projections in the complex Euclidean space, and the corresponding phase retrieval algorithms proceed by projecting the estimated wavefield back in an iterative manner^{33,34}. Since the seminal Gerchberg-Saxton³⁵ and Fienup's error-reduction algorithms³⁶, iterative projection algorithms have played a pivotal role in phase retrieval for decades^{37–39}. However, this classical approach relies on carefully handcrafted physical constraints, which may fail to fully extract the inherent features of complex scenes under limited measurements, particularly in the case of single-shot phase retrieval⁴⁰. Consequently, it has mostly been demonstrated for simple objects. The quantitative phase analysis of complex samples, such as dense biological specimens, remains a challenging task.

The concept of compressive phase retrieval was formally established by an explosion of theoretical and empirical studies following the development of compressed sensing^{41–43}. Sparsity priors in various domains such as the spatial^{44–49}, gradient^{50–61}, wavelet⁶² and other domains^{63,64} or with a dictionary-learned transform^{65–67} have been demonstrated as effective regularizers for phase recovery. More recently, implicit image priors from advanced denoisers such as BM3D^{68–73} or represented by deep neural networks^{74–93} have also been studied in the context of phase retrieval, resulting in improved reconstruction quality. Although the regularization techniques generally yield

superior imaging performance, they are highly dependent on the scene and may require manual fine-tuning to achieve satisfactory results.

In pursuit of a compressive phase retrieval method for in-line holography that features both robustness and high fidelity, we propose a novel computational framework that encapsulates physical constraints and sparsity priors as a unified optimization problem. Specifically, we consider the well-known absorption and support constraints and gradient-domain sparsity, leading to a constrained complex total variation (CCTV) model. This is because TV-regularized problems can be solved using computationally efficient algorithms and are thus highly scalable to large-scale problems^{94,95}. The piece-wise smoothness underlying the TV model can also characterize multidimensional data such as the three-dimensional refractive index distribution, offering good generalizability to various applications^{96–99}. Furthermore, TV-regularized inversion algorithms offer mathematically tractable convergence behaviors, which is important for both theoretical soundness and practical implementation.

Based on the CCTV model, compressive phase retrieval is formulated as a regularized inverse problem and is solved via an accelerated proximal gradient algorithm together with an efficient denoiser for the proximal update. Unlike conventional methods that rely on a heuristic basis, we provide a rigorous mathematical analysis that guarantees the convergence of the proposed algorithms using prespecified parameters. We experimentally demonstrated quantitative phase imaging of various samples from a single in-line hologram, illustrating the effectiveness of the CCTV model in characterizing complex real-world scenes while leveraging physically tractable constraints for quality enhancement. We further elaborate on algorithmic behaviors based on extensive numerical studies, corroborating the theoretical results while providing general guidance for practitioners.

Results

Phase retrieval via CCTV

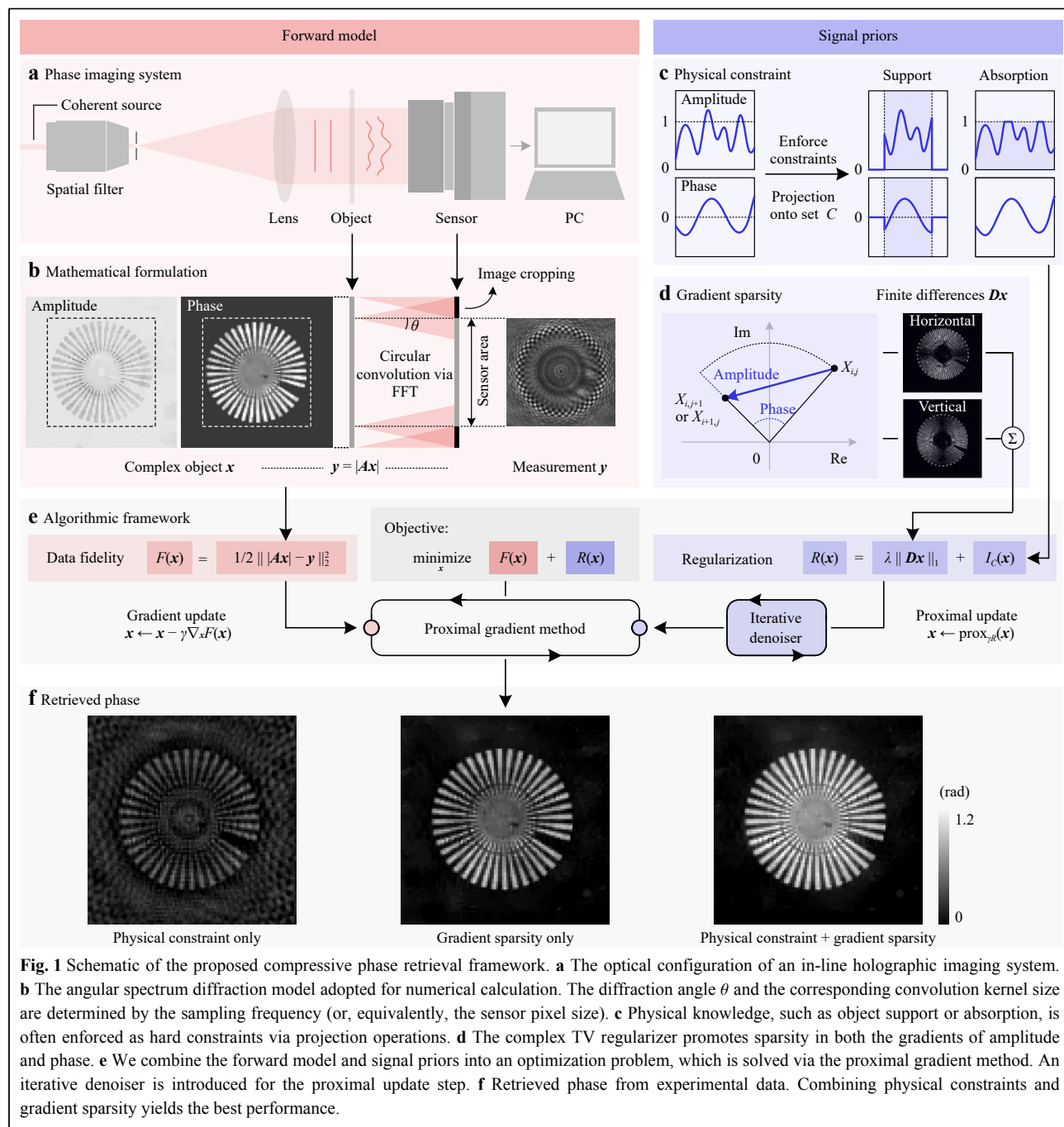
For electromagnetic waves at optical frequencies, sensors can only respond to the average power of the incident wavefield. Thus, phase information, i.e., the complex argument of the signal, is lost during the measurement process. The forward model can be abstractly expressed, regardless of the imaging configuration, in a vectorized form as

$$\mathbf{y} = |\mathbf{Ax}| \quad (1)$$

where $\mathbf{y} \in \mathbb{R}^m$ is the observed measurement, $\mathbf{A} \in \mathbb{C}^{m \times n}$ is the

sampling matrix, and $\mathbf{x} \in \mathbb{C}^n$ is the underlying complex signal that represents the transmission of the object. In the vectorized formulation, column vectors \mathbf{x} and \mathbf{y} are raster-scanned from the corresponding two-dimensional complex object transmission function and hologram amplitude, respectively. It is important to note that, the purpose of vectorization is to simplify the algorithm derivation and notations. Vectorization is not required when implementing the algorithm in practice.

Generally, the sampling matrix may involve various linear physical processes such as probe illumination, free-space propagation and mask modulation, all of which are determined by the optical configuration of the imaging system. In this work, we consider the lensless in-line holographic imaging model for illustration, which is shown in Fig. 1a. The object is illuminated by a coherent plane wave, such that the retrieved complex field directly reveals the absorption and phase shift introduced by the object. An



imaging sensor was placed close to the object, and the in-line hologram was recorded. Such a simple optical configuration enables low-cost and portable system design for various imaging applications^{100,101}. The physical process involves only free-space propagation of the wavefield, which is calculated using the angular spectrum method¹⁰². Therefore, the sampling matrix of our imaging model can be expressed as

$$\mathbf{A} = \mathbf{CQ} \quad (2)$$

where $\mathbf{Q} \in \mathbb{C}^{n \times n}$ denotes the free-space propagation operator calculated as a circular convolution with the Fresnel kernel via fast Fourier transforms (FFTs), $\mathbf{C} \in \mathbb{R}^{m \times n}$ denotes an image cropping operation to model the finite size of the imaging sensor¹⁰³. Notice that we have $m < n$, that is, the object dimension is larger than the pixel number of the sensor. This is because out-of-field objects may also contribute to the recorded image owing to the linear convolution effect⁵⁴. This process is illustrated in Fig. 1b.

Phase reconstruction from a single in-line hologram is inherently challenging due to the existence of ambiguous solutions. Therefore, compressive phase retrieval takes an inverse problem approach that utilizes regularization techniques to ensure well-posedness. In this work, we introduce the integration of a complex TV and a hard constraint as the regularizer, leading to an optimization problem in the following form:

$$\min_{\mathbf{x}} \underbrace{\frac{1}{2} \| |\mathbf{Ax}| - \mathbf{y} \|_2^2}_{F(\mathbf{x})} + \underbrace{\lambda \| \mathbf{Dx} \|_1 + I_C(\mathbf{x})}_{R(\mathbf{x})} \quad (3)$$

where $\|\cdot\|_p$ denotes the ℓ_p vector norm or the corresponding matrix norm. $F(\mathbf{x})$ is the data-fidelity term and $R(\mathbf{x})$ is the regularization term. The fidelity term ensures that the solution does not deviate significantly from the forward model in Eq. 1. Meanwhile, the regularization term introduces additional prior knowledge of the wavefield to improve the reconstruction quality further.

There are various choices for the fidelity function $F(\mathbf{x})$ in the phase retrieval literature, such as the intensity-based formulation $F(\mathbf{x}) = (1/2) \| |\mathbf{Ax}|^2 - \mathbf{y}^2 \|_2^2$ ^{104–106} and the amplitude-based formulation $F(\mathbf{x}) = (1/2) \| |\mathbf{Ax}| - \mathbf{y} \|_2^2$ ^{107–109}. The main reasons for choosing the amplitude-based residual here are threefold. First, from a physical perspective, it is closely related to the maximum likelihood estimation under Poisson noise, which captures the noise statistics more accurately than the Gaussian noise model¹¹⁰. Second, on the practitioner's side, using the amplitude-based formulation ensures the convergence of the iterative algorithms with a prespecified algorithm step size, obviating the need for complicated line searches and

simplifying the implementation. Third, many empirical studies have observed faster convergence when minimizing amplitude-based fidelity functions^{111,112}.

The proposed regularization function $R(\mathbf{x})$ comprises two separate terms. The first term is the sparsity regularizer with the parameter $\lambda > 0$. Specifically, we considered the anisotropic complex TV seminorm:

$$\| \mathbf{Dx} \|_1 = \text{TV}(\mathbf{X}) = \sum_{i=1}^{n_\xi-1} \sum_{j=1}^{n_v} |X_{i+1,j} - X_{i,j}| + \sum_{i=1}^{n_\xi} \sum_{j=1}^{n_v-1} |X_{i,j+1} - X_{i,j}| \quad (4)$$

where $\mathbf{X} \in \mathbb{C}^{n_\xi \times n_v}$ with $n_\xi n_v = n$ denotes the non-vectorized two-dimensional image corresponding to \mathbf{x} . $\mathbf{D} \in \mathbb{C}^{2n \times n}$ denotes the spatial finite-difference operator for the vectorized \mathbf{x} along the two directions. As shown in Fig. 1d, the complex TV reveals both the amplitude and phase variations between adjacent sampling points of the object transmission function and thus serves as a good sparsifying transform for complex-valued images¹¹³. Apart from the complex TV, we introduce a second regularizer $I_C(\mathbf{x})$, which is an indicator function of the constraint set C . This is motivated by conventional iterative projection (IP) phase retrieval algorithms, where phase retrieval is formulated as a feasibility problem, and the unknown field distribution is assumed to belong to certain physical constraint sets. The IP algorithms typically proceed by projecting the estimated wavefield onto constraint sets in an iterative manner^{37,38}. Here, we consider the support and absorption constraints in particular because they are commonly adopted for reconstructing complex objects, and their corresponding constraint sets are both convex. Fig. 1c presents a conceptual illustration of these physical constraints, and the mathematical definitions are presented in Table 1. The proposed regularizer $R(\mathbf{x})$ comprises a complex TV and a hard physical constraint and is thus termed the constrained complex total variation regularizer. As a special case, when $C = \mathbb{C}^n$, CCTV reduces to the complex TV function without physical constraints, and when $\lambda = 0$, it reduces to

Table 1 Physical constraints for phase retrieval

Constraint	Definition of C	Projection $\mathbf{x}' = \mathcal{P}_C(\mathbf{x})$
Support	$\mathbf{x} \odot \mathbf{1}_P = \mathbf{0}$	$x'_i = \begin{cases} 0, & i \in P \\ x_i, & i \notin P \end{cases}$
Absorption	$ \mathbf{x} \leq \mathbf{1}$	$x'_i = \begin{cases} x_i / x_i , & x_i > 1 \\ x_i, & x_i \leq 1 \end{cases}$

¹ The symbol \odot denotes the element-wise (Hadamard) multiplication operator. $\mathbf{0}$ and $\mathbf{1}$ denote the zero vector and all-ones vector, respectively. P denotes the set of pixels outside the support region, and $\mathbf{1}_P$ denotes the indicator vector of P .

the classical problem of phase retrieval from a modulus measurement and a physical constraint.

Quantitative phase imaging applications

We built a proof-of-principle in-line holographic imaging system for optical experiments, as shown in Fig. 2a. A 660 nm diode-pumped solid-state laser (Cobolt Flamenco 300) was used as the source for coherent illumination. The optical beam generated by the laser passes through a spatial filter that comprises an objective lens and a pinhole at the back focal plane. The filtered wave was then collimated using a convex lens to illuminate

the object. The diffraction pattern was recorded using a CMOS sensor (QHY174GPS, pixel size 5.86 μm , resolution 1920×1200) which was placed a few millimeters away from the object. The captured raw intensity image was then digitally processed using a personal computer for holographic reconstruction. In all optical experiments, we consider only the absorption constraint because the objects have extended field distributions and thus the support constraint is inapplicable. Before running the iterative phase retrieval algorithm, a preprocessing step is required to determine the imaging distance, which can be achieved by either manual tuning or using some autofocusing

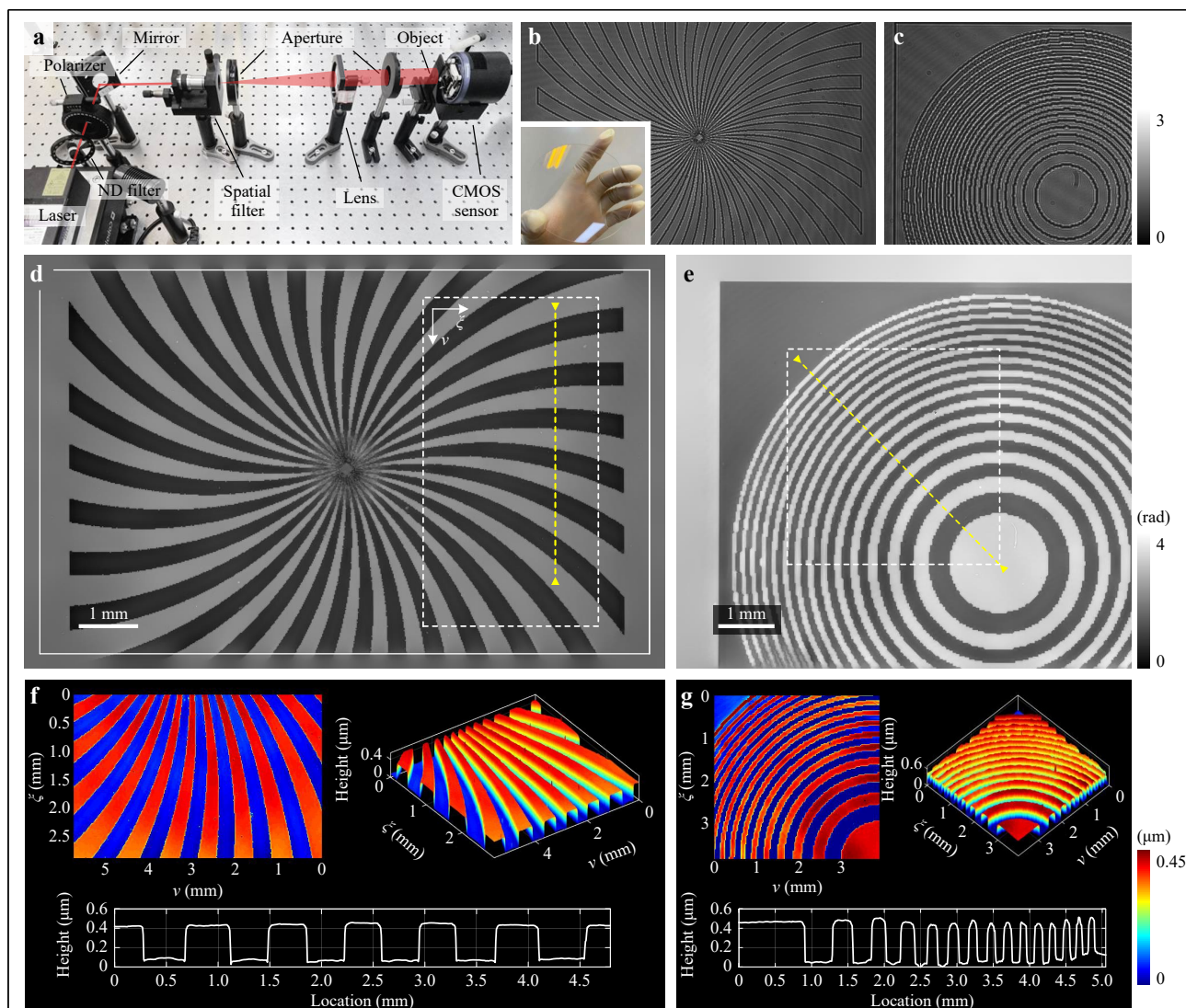


Fig. 2 Experimental characterization of a fabricated phase plate. **a** Optical setup of the in-line holographic imaging system. **b** and **c** show the captured in-line holograms of two transparent patterns. The inset shows an image of the phase plate. **d** and **e** show the reconstructed phase distribution from **b** and **c**, respectively. The white solid rectangle in **d** indicates the sensor's field of view. **f** and **g** visualize the rendered surface profiles and the cross-sectional height profiles of **d** and **e**, respectively. The white dashed rectangles indicate the enlarged areas, and the yellow dashed lines indicate the cross-sections. The same applies to other figures.

algorithms^{114–116}. Each captured intensity image is normalized by the background image which is obtained using the same experimental conditions, only with the object removed. This calibration process ensures the validity of the absorption constraint³⁹.

We demonstrated the quantitative phase imaging capability of the proposed compressive phase retrieval method for real-world objects. Fig. 2 shows the imaging results of a phase plate, which was fabricated by etching multiple self-designed binary patterns onto a JGS1 quartz glass substrate. The retrieved phases of the spiral pattern and Fresnel zone plate are shown in Fig. 2d, e, respectively. Smooth staircase profiles with sharp edges can be accurately retrieved. Artifacts on the surface were preserved, indicating a high spatial resolution. Given that the object has a uniform refractive index distribution and that the fabricated features lie only on the surface of the substrate, the surface profiles can be directly calculated and characterized with knowledge of the medium refractive index, as shown in Fig. 2f, g. It is important to note that recovering the low-frequency phase is inherently challenging for the in-line configuration because the weak phase transfer function diminishes to zero together with the spatial frequency¹¹⁷. Hence, slowly varying phase structures hardly contribute to the intensity variations at the sensor plane, rendering them particularly difficult to recover. This has been the main drawback for in-line holography compared to off-axis holography^{118,119}. Our findings suggest that the CCTV regularizer may be a competitive solution for this problem. In addition, because we have addressed the issue of the circular convolution model, the retrieved image is free from boundary artifacts, and the object distribution outside the sensor area can be partially recovered, as shown in Fig. 2d.

We imaged a muscle tissue section to validate the proposed method on complex objects, as shown in Fig. 3. The twin image was effectively eliminated from the retrieved amplitude and phase, which visually demonstrated the high-fidelity imaging performance of the method. The retrieved phase reveals thickness variations inside the tissue slice, facilitating label-free and low-cost clinical studies or diagnoses^{120,121}.

Ablation experiments

We conducted ablation studies based on experimental data to quantify the performance improvements obtained by the physical constraints and the complex TV regularizer respectively. For comparison, we implemented compressive phase retrieval algorithms using only physical constraints or gradient sparsity. The former, referred to as the IP method, can be viewed as an accelerated variant of the conventional iterative projection algorithm. This was implemented by setting the regularization parameter $\lambda = 0$. The algorithm proceeds by iteratively minimizing the data-fidelity function with a gradient descent step and enforcing physical constraints with a projection step. The latter, referred to as the CTV method, uses only the complex TV regularizer without any physical constraints. It is implemented by defining the constraint set $C = \mathbb{C}^n$ and thus the projection onto set C is reduced to identity mapping.

Both the IP and CCTV methods can utilize various physical constraints. To better differentiate among different methods, we use the letter ‘A’ to represent the method that uses the absorption constraint, the letter ‘S’ for the support constraint, and ‘AS’ for both constraints. For example, ‘IP-A’ represents an iterative projection algorithm that uses only the absorption constraint.

We first performed phase imaging of a quantitative

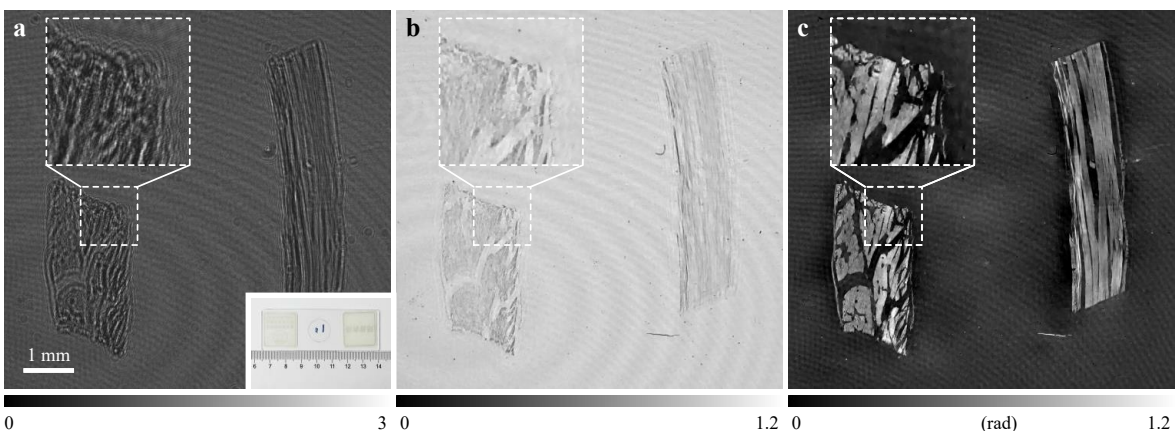


Fig. 3 Holographic imaging results of a muscle tissue section. **a** Experimentally recorded intensity image. The inset is an image of the sample slide. **b** and **c** are the retrieved amplitude and phase, respectively.

phase microscopy target (Benchmark Technologies) using three methods, namely IP-A, CTV, and CCTV-A, as shown in Fig. 4. Note that the object has an extended distribution and thus the support constraint is inapplicable. The IP algorithm fails to eliminate the twin-image artifact completely, and the phase structures are not clearly revealed, which implies that the physical constraint alone is

insufficient to suppress the phase ambiguities. The CCTV method achieved better imaging quality than CTV, as illustrated by visual and quantitative comparisons. The ground-truth phase values were calculated using the structures' height and medium refractive index, which are both provided by the manufacturer. The root-mean-square errors (RMSEs) of the cross-sectional phase profiles

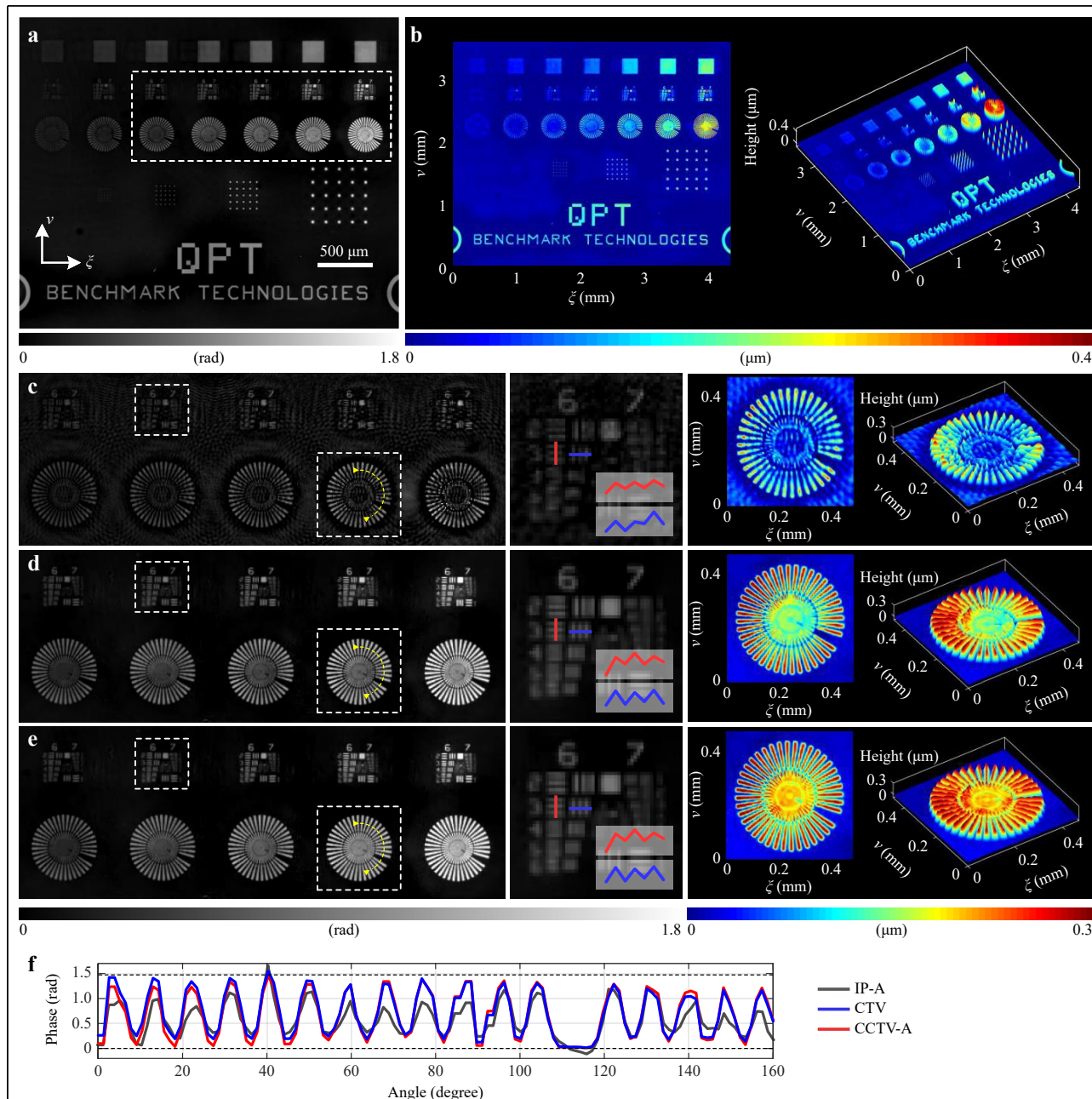


Fig. 4 Experimental comparison of different phase retrieval algorithms with a quantitative phase resolution target. **a** Full field-of-view phase reconstruction by the proposed CCTV-A method. **b** The calculated surface profile corresponding to **a**. **c**, **d** and **e** show the retrieved phase and height profiles by the IP-A, CTV, and CCTV-A methods, respectively. **f** The cross-sectional phase profiles, where the dashed line indicates the calculated theoretical phase value.

retrieved using the IP-A, CTV, and CCTV-A methods were 0.880, 0.463, and 0.418 rad, respectively. In addition, the finest resolved features of the USAF 1951 resolution target are highlighted. Group 6, Element 3 is resolved by all three methods, indicating a spatial resolution of 80.6 lines/mm, which agrees with the maximum resolution of 85.3 lines/mm of the sensor. All three methods achieve the same sampling-limited resolution, which implies that the TV-based regularizer does not sacrifice the spatial resolution for quality enhancement. The resolution can be further improved beyond the Nyquist sampling limit, however, if one takes into account the down-sampling effect of the sensor pixels^[112,122–126].

Similar improvements in the CCTV method over the IP and CTV methods were also observed in the imaging results of an amplitude object. Fig. 5 compares the amplitudes of a positive 1951 USAF test target (Thorlabs, Inc.) retrieved by the IP-A, CTV, and CCTV-A methods.

Quantitatively, the RMSEs of the retrieved amplitude profiles 1/2 in Fig. 5d are 0.331/0.338, 0.240/0.239, 0.238/0.232 for the IP-A, CTV and CCTV-A methods, respectively. Furthermore, as indicated by a qualitative visual comparison, the IP method suffers from high reconstruction noise, and the CCTV model improves the performance of CTV by suppressing artifacts with no loss of spatial resolution.

Materials and methods

The proximal gradient framework

In the regularized inverse problem of Eq. 3, the fidelity function $F(\mathbf{x})$ is a (almost everywhere) differentiable function whereas the regularizer $R(\mathbf{x})$ is a non-differentiable function. Because we are dealing with real-valued functions over complex-valued variables, CR-calculus is adopted^[127]. The gradient of $F(\mathbf{x})$ is given by^[112]

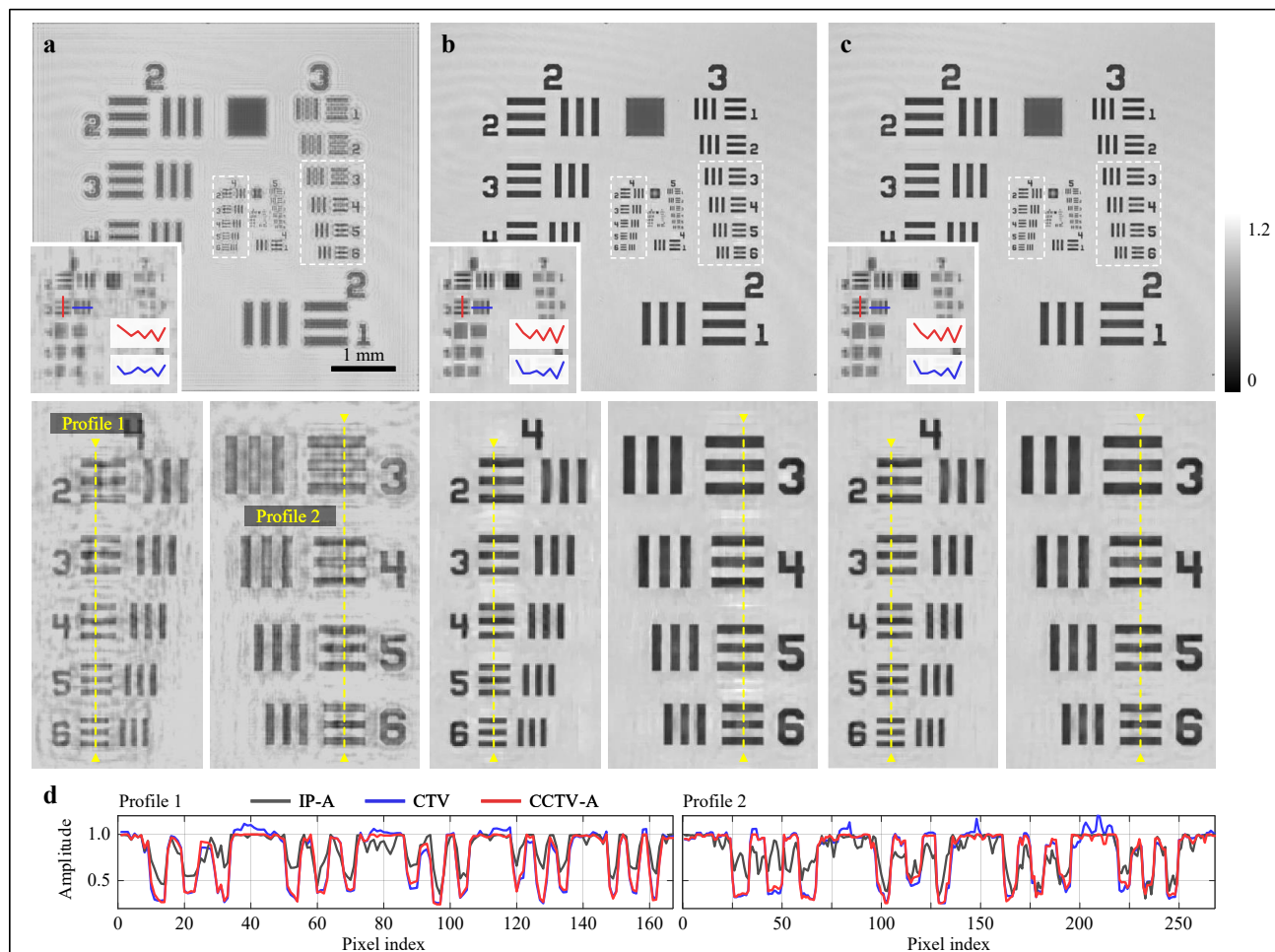


Fig. 5 Experimental comparison of different phase retrieval algorithms with an amplitude resolution target. **a, b** and **c** show the retrieved amplitude using the IP-A, CTV, and CCTV-A algorithms, respectively. The inset indicates the finest structures resolved by the corresponding method. Below are the corresponding enlarged areas. **d** Cross-sectional profiles.

$$\nabla_x F(\mathbf{x}) = \frac{1}{2} A^H \text{diag}\left(\frac{A\mathbf{x}}{|A\mathbf{x}|}\right)(|A\mathbf{x}| - \mathbf{y}) \quad (5)$$

where $(\cdot)^H$ denote the conjugate transpose (Hermitian) operator. Non-smoothness only occurs when $A\mathbf{x}$ has zero entries, which, as we will show below, does not affect the algorithm's convergence behavior.

The difficulty in minimizing the objective function mainly arises from the non-differentiability of $R(\mathbf{x})$. The proximal gradient method provides a general framework for solving composite non-smooth optimization problems in the form of Eq. 3 by minimizing the non-differentiable $R(\mathbf{x})$ via its proximal operator $\text{prox}_{\gamma R}$, which is defined as¹²⁸

$$\text{prox}_{\gamma R}(\mathbf{v}) = \underset{\mathbf{x}}{\operatorname{argmin}} R(\mathbf{x}) + \frac{1}{2\gamma} \|\mathbf{x} - \mathbf{v}\|_2^2 \quad (6)$$

where $\gamma > 0$ is the step size. Notice that Eq. 6 coincides with an image denoising problem, with $R(\mathbf{x})$ serving as a regularization function. For the CCTV regularizer, the denoising subproblem can be solved efficiently using the gradient projection algorithm introduced in the next subsection. The proximal gradient algorithm proceeds by iteratively applying a gradient update and proximal update. A variant using the Nesterov's acceleration technique was adopted¹²⁹, as shown in Algorithm 1. The accelerated proximal gradient (APG) algorithm is also known as the fast iterative shrinkage thresholding algorithm (FISTA)¹³⁰. APG is well known for its superior convergence speed over the basic proximal gradient algorithm in the convex setting. Through numerical studies, we empirically demonstrate that it also helps to speed up convergence for the nonconvex phase retrieval problem.

Algorithm 1 Accelerated proximal gradient algorithm

Input: Initial guess $\mathbf{x}^{(0)}$, step size γ , $\beta_t = t/(t+3)$, and iteration number T .

```

1:  $\mathbf{u}^{(0)} = \mathbf{x}^{(0)}$ 
2: for  $t = 1, 2, \dots, T$  do
3:    $\mathbf{v}^{(t)} = \mathbf{u}^{(t-1)} - \gamma \nabla_{\mathbf{u}} F(\mathbf{u}^{(t-1)})$            ▷ Gradient update
4:    $\mathbf{x}^{(t)} = \text{prox}_{\gamma R}(\mathbf{v}^{(t)})$                    ▷ Proximal update via Alg. 2
5:    $\mathbf{u}^{(t)} = \mathbf{x}^{(t)} + \beta_t(\mathbf{x}^{(t)} - \mathbf{x}^{(t-1)})$ 
6: end for

```

CCTV denoising algorithm

The proximal update step in Eq. 6 involves solving a CCTV-regularized image denoising subproblem. It is a convex optimization problem when C is closed and convex. No exact closed-form solution to this problem is available. Thus, an iterative solver should be invoked at every iteration. We followed the approach proposed in Refs. 95,131 and consider solving the primal problem via its

dual, which is given by

$$\min_{\mathbf{w} \in S} \{G(\mathbf{w}) \equiv -\|\mathcal{H}_C(\mathbf{v} - \gamma \mathbf{D}^H \mathbf{w})\|_2^2 + \|\mathbf{v} - \gamma \mathbf{D}^H \mathbf{w}\|_2^2\} \quad (7)$$

where $\mathbf{w} \in \mathbb{C}^{2n}$ denotes the dual variable, $\mathcal{H}_C(\mathbf{x}) \stackrel{\text{def}}{=} \mathbf{x} - \mathcal{P}_C(\mathbf{x})$ with \mathcal{P}_C representing the Euclidean projection operator on C , and S denotes the convex set which contains all $\mathbf{w} \in \mathbb{C}^{2n}$ that satisfy

$$\|\mathbf{w}\|_\infty \leq \lambda \quad (8)$$

where $\|\mathbf{w}\|_\infty = \max_i |w_i|$. As shown in the Supplementary Document, the desired primal optimal solution \mathbf{x}^* is related to the dual optimal solution \mathbf{w}^* through the following equation:

$$\mathbf{x}^* = \mathcal{P}_C(\mathbf{v} - \gamma \mathbf{D}^H \mathbf{w}^*) \quad (9)$$

The problem of Eq. 7 can be effectively solved using the gradient projection algorithm, where the dual variable is iteratively updated by a gradient step followed by a projection operation $\mathcal{P}_S(\cdot)$ onto the set S . An accelerated variant of the algorithm is presented in Algorithm 2. The Wirtinger gradient of the dual objective function $G(\mathbf{w})$ is given by¹³¹

$$\nabla_{\mathbf{w}} G(\mathbf{w}) = -\gamma \mathbf{D} \mathcal{P}_C(\mathbf{v} - \gamma \mathbf{D}^H \mathbf{w}) \quad (10)$$

Algorithm 2 Accelerated gradient projection algorithm

Input: Observation \mathbf{v} , parameter γ , step size η , $\beta_t = t/(t+3)$, and subiteration number T_{sub} .

```

1:  $\mathbf{w}^{(0)} = \mathbf{0}$ ,  $\mathbf{z}^{(0)} = \mathbf{w}^{(0)}$ 
2: for  $t = 1, 2, \dots, T_{\text{sub}}$  do
3:    $\mathbf{w}^{(t)} = \mathcal{P}_S \left( \mathbf{z}^{(t-1)} - \eta \nabla_{\mathbf{z}} G(\mathbf{z}^{(t-1)}) \right)$ 
4:    $\mathbf{z}^{(t)} = \mathbf{w}^{(t)} + \beta_t(\mathbf{w}^{(t)} - \mathbf{w}^{(t-1)})$ 
5: end for
6:  $\mathbf{x} = \mathcal{P}_C(\mathbf{v} - \gamma \mathbf{D}^H \mathbf{w}^{(T_{\text{sub}})})$ 

```

Convergence analysis

In the above subsections, we introduce the proximal gradient algorithm and the corresponding denoising algorithm for the proximal update. We now show that the algorithm parameters, namely the step sizes γ and η , can be predetermined based on the measurement scheme and the sparsifying transform.

Considering the nonconvexity of the problem of Eq. 3, we present a weaker result by showing the convergence of the basic (non-accelerated) proximal gradient algorithm, which is summarized by the following theorem. The detailed proof is provided in the Supplementary Document. Furthermore, extensive numerical studies have demonstrated that the accelerated algorithm converges following the same step size selection rule.

Theorem 1 *The basic proximal gradient algorithm (with $\beta_t \equiv 0$ in Algorithm 1) for the problem of Eq. 3 converges to*

a stationary point using a fixed step size γ that satisfies

$$\gamma \leq \frac{2}{\rho(\mathbf{A}^H \mathbf{A})} \quad (11)$$

where $\rho(\cdot)$ denotes the spectral radius.

The above theorem is an extension of the gradient descent algorithm¹³² to the more general class of the proximal gradient algorithms.

The sampling matrix \mathbf{A} depends only on the physical model. Thus, the step size can be known a priori. Recall that the sampling matrix comprises a circular convolution operator \mathbf{Q} and an image cropping operator \mathbf{C} . Circular convolution can be efficiently calculated via FFTs as $\mathbf{Q} = \mathbf{F}^{-1} \text{diag}(\mathbf{h}) \mathbf{F}$, where \mathbf{F} is the Fourier matrix and \mathbf{h} is the transfer function. Note that $|\mathbf{h}| = 1$. Thus, \mathbf{Q} is a unitary matrix that satisfies $\mathbf{Q}^H \mathbf{Q} = \mathbf{I}$, where \mathbf{I} is the identity matrix. It can be easily verified that $\rho(\mathbf{A}^H \mathbf{A}) \leq 1$, which, according to Theorem 1, implies that we should use step size $\gamma = 2$ for the proximal gradient algorithm. This choice of step size is in fact nontrivial and generally applicable to any passive measurement scheme.

The next theorem establishes the convergence of the accelerated gradient projection algorithm to solve the convex denoising subproblem via its dual (Eq. 7). The proof can be found in the Supplementary Document.

Theorem 2 Assuming that the constraint set \mathcal{C} is closed and convex, the accelerated gradient projection algorithm for the problem of Eq. 7 converges to the global optimum using a fixed step size η that satisfies

$$\eta \leq \frac{1}{\gamma^2 \rho(\mathbf{D}^H \mathbf{D})} \quad (12)$$

Theorem 2 suggests that the step size for the denoising algorithm can also be determined beforehand based on γ given by Theorem 1 and the sparsifying transform \mathbf{D} . Specifically, for the finite-difference operator, we show in the Supplementary Document that $\rho(\mathbf{D}^H \mathbf{D}) \leq 8$, which, together with $\gamma = 2$, suggests $\eta = 1/32$ for this particular case. The convergence established by Theorem 1 assumes that an exact solution to the denoising subproblem is obtained at each iteration. The algorithm may converge to a suboptimal solution when the proximal update is inexact, as with the CCTV regularizer. Readers can refer to Ref. 133 and references therein for convergence results regarding inexact proximal gradient algorithms. Therefore, the iteration number used for the gradient projection algorithm should be chosen as a balance between reconstruction quality and computation efficiency.

Discussion

We performed numerical studies based on the same inline holographic imaging model as described in the

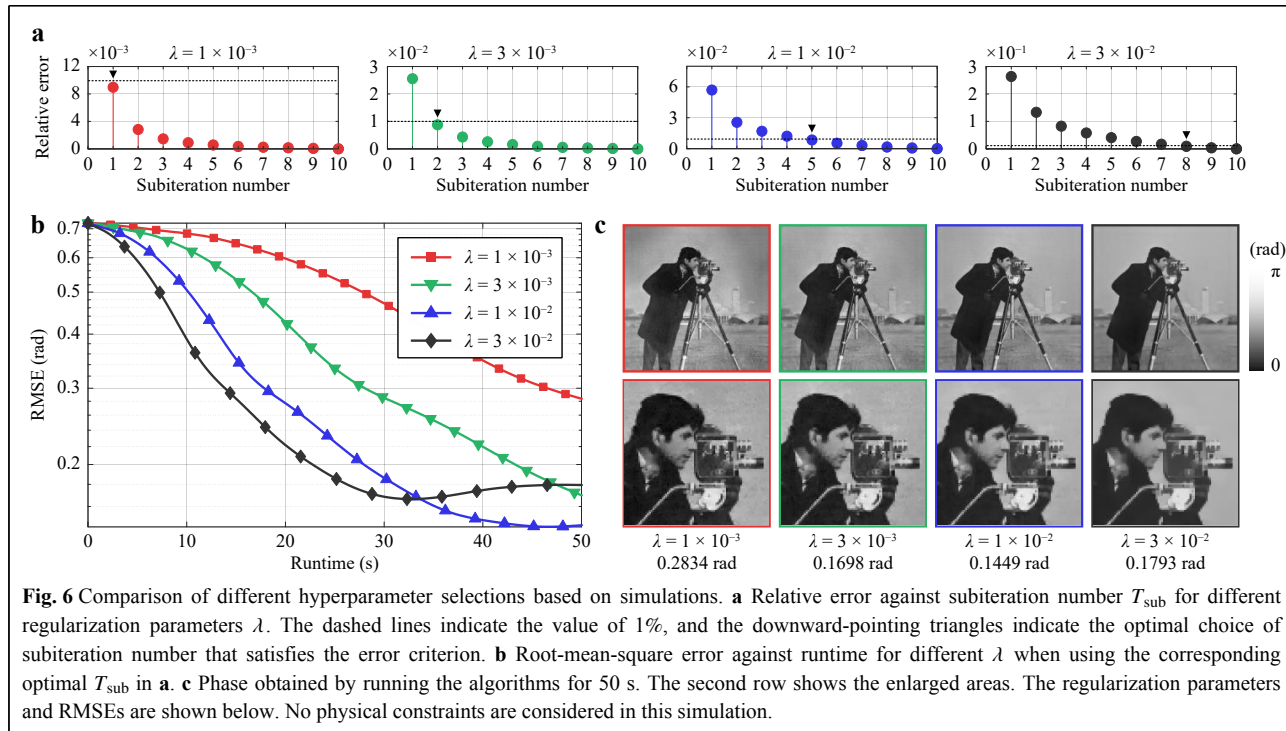
experiment section to quantitatively evaluate the algorithmic behaviors and further shed light on our empirical observations and theoretical results. The wavelength was set to 500 nm, the pixel size was 5 μm , and the imaging distance was 5 mm. Eight standard test images of size 256×256 were used to generate the virtual phase objects for the simulation. The phase of the object was assumed to have a range of $[0, \pi]$. The objects have a uniform amplitude distribution and were zero-padded to avoid boundary artifacts. Additive white Gaussian noise was added to each hologram such that the signal-to-noise ratio (SNR) was 20 dB by default. We calculated the phase RMSE as a metric to quantitatively compare the reconstruction quality of different methods.

In all numerical studies, the algorithms were initialized with an initial estimate of $\mathbf{x}^{(0)} = \mathbf{A}^H \mathbf{y}$. The algorithms were implemented using MATLAB on a personal computer with Core i7-11700F CPU @ 2.50GHz (Intel) and 16 GB of RAM. The MATLAB code is publicly available in Ref. 134.

Hyperparameter selection

We first investigated the influence of the subiteration number T_{sub} of the gradient projection denoising algorithm on the convergence of the proximal gradient algorithm. As previously pointed out, T_{sub} is a key hyperparameter that should be determined beforehand. We ran the APG algorithm for 1000 iterations using different T_{sub} values ranging from one to ten. Meanwhile, four regularization parameters, $\lambda = 1 \times 10^{-3}$, 3×10^{-3} , 1×10^{-2} , and 3×10^{-2} were considered for comparison. To quantify the convergence behavior of the inexact APG algorithms, we calculated the relative error of the final objective function value for each T_{sub} relative to that with $T_{\text{sub}} = 10$. Fig. 6a indicates that the relative error decreases monotonically as T_{sub} increases, and thus, a more accurate proximal update can be obtained by increasing the number of subiterations. We empirically selected the smallest T_{sub} that yielded an error below 1% as the optimal choice. Another observation made from Fig. 6a is the dependence of T_{sub} on regularization parameter λ . As λ increases, one needs more subiterations for the denoising algorithm to obtain an adequate solution. This seems quite natural, considering the nonlinear nature of the denoising operation. A larger λ imposes a stronger regularization force on the image, thus requiring more linear iterative steps to approximate the solution.

Another hyperparameter of great importance is the regularization parameter λ , which offers a tradeoff between model consistency and signal priors. We compared different selections of λ in terms of both the reconstruction quality and computational efficiency. Fig. 6b plots the



convergence curves against runtime, where the optimal T_{sub} was used for each λ , that is, $T_{\text{sub}} = 1$ for $\lambda = 1 \times 10^{-3}$, $T_{\text{sub}} = 2$ for $\lambda = 3 \times 10^{-3}$, $T_{\text{sub}} = 5$ for $\lambda = 1 \times 10^{-2}$, and $T_{\text{sub}} = 8$ for $\lambda = 3 \times 10^{-2}$. A larger regularization parameter can help accelerate the convergence at the beginning stage. However, the final result tends to be over-smoothed, as shown in Fig. 6c. Therefore, we set $\lambda = 1 \times 10^{-2}$ for balanced performance in terms of speed and accuracy.

Comparison of physical constraints

Having determined the optimal hyperparameters for the complex TV, we evaluated the effect of incorporating additional physical constraints. Fig. 7 shows the results obtained using no constraints, support constraint, absorption constraint, or both. For the support constraint, the support region was set to the central 256×256 pixels of the image. The introduction of the absorption constraint can significantly improve the overall quality, while the support constraint can help suppress artifacts at the boundaries. Incorporating physical constraints also helps accelerate convergence.

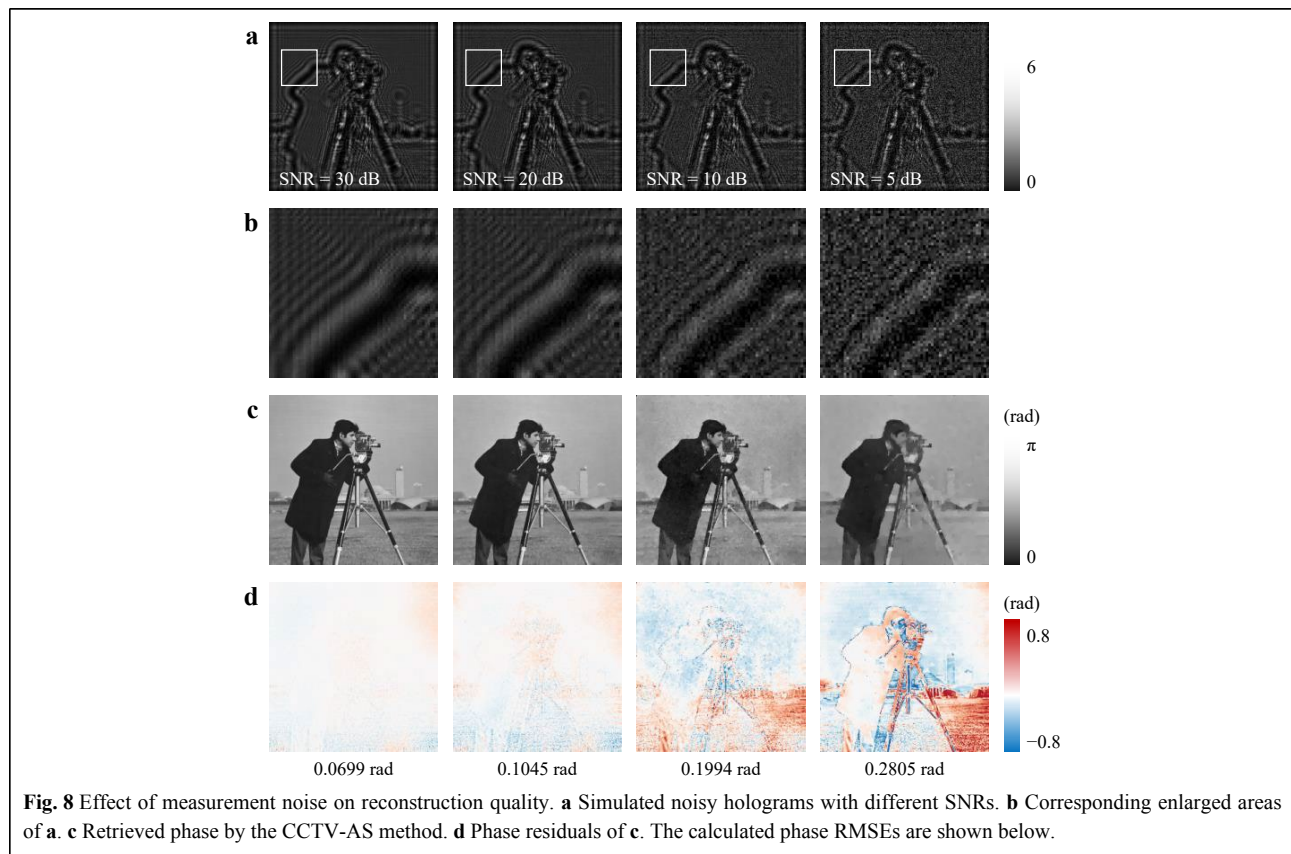
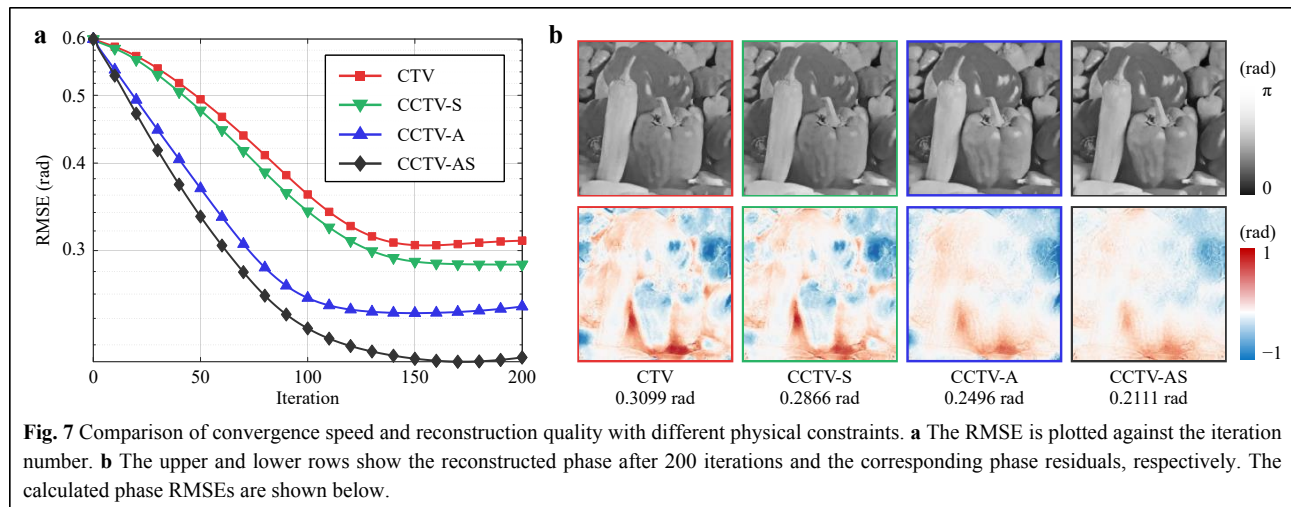
Influence of measurement noise

The inherent ill-posedness of single-shot phase retrieval leads to high sensitivity to measurement noise. To quantitatively compare the phase reconstruction quality under noisy conditions, we added different levels of additive white Gaussian noise with an SNR ranging from 5

to 30 dB to the simulated hologram, as shown in Fig. 8a. The corresponding phases retrieved by the CCTV-AS method are presented in Fig. 8c. The CCTV method can achieve high-quality phase retrieval under moderate-noise conditions. However, when the hologram is severely degraded by measurement noise, a larger regularization parameter λ is required to suppress reconstruction artifacts. The retrieved phase may then exhibit a staircase artifact when the regularization parameter is too large, which is an inherent problem for TV-based regularizers. Therefore, more advanced image priors are required to achieve better reconstruction quality under noisy conditions.

Generalization to different scenes

To further examine the generalizability of the CCTV model, we tested the algorithm on various test images and compared it with IP and CTV methods. The results are shown in Fig. 9. The conventional IP algorithm generally suffers from a high reconstruction error because the physical constraints alone are insufficient to suppress the twin-image artifact. On the other hand, the CTV model often yields visually appealing results, yet its performance is highly dependent on the sparsity of the scene. For example, the CTV model tends to perform well for scenes with very sparse gradients, such as the *House* image, but it may be unsuitable for retrieving complex scenes, such as the *Goldhill* and *Mandrill* images. In all cases, the CCTV model offers the best reconstruction quality owing to the

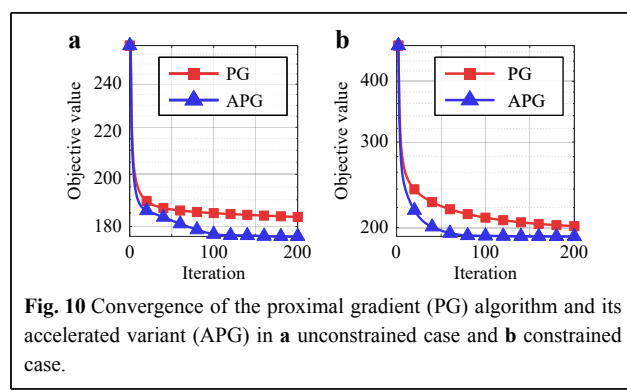
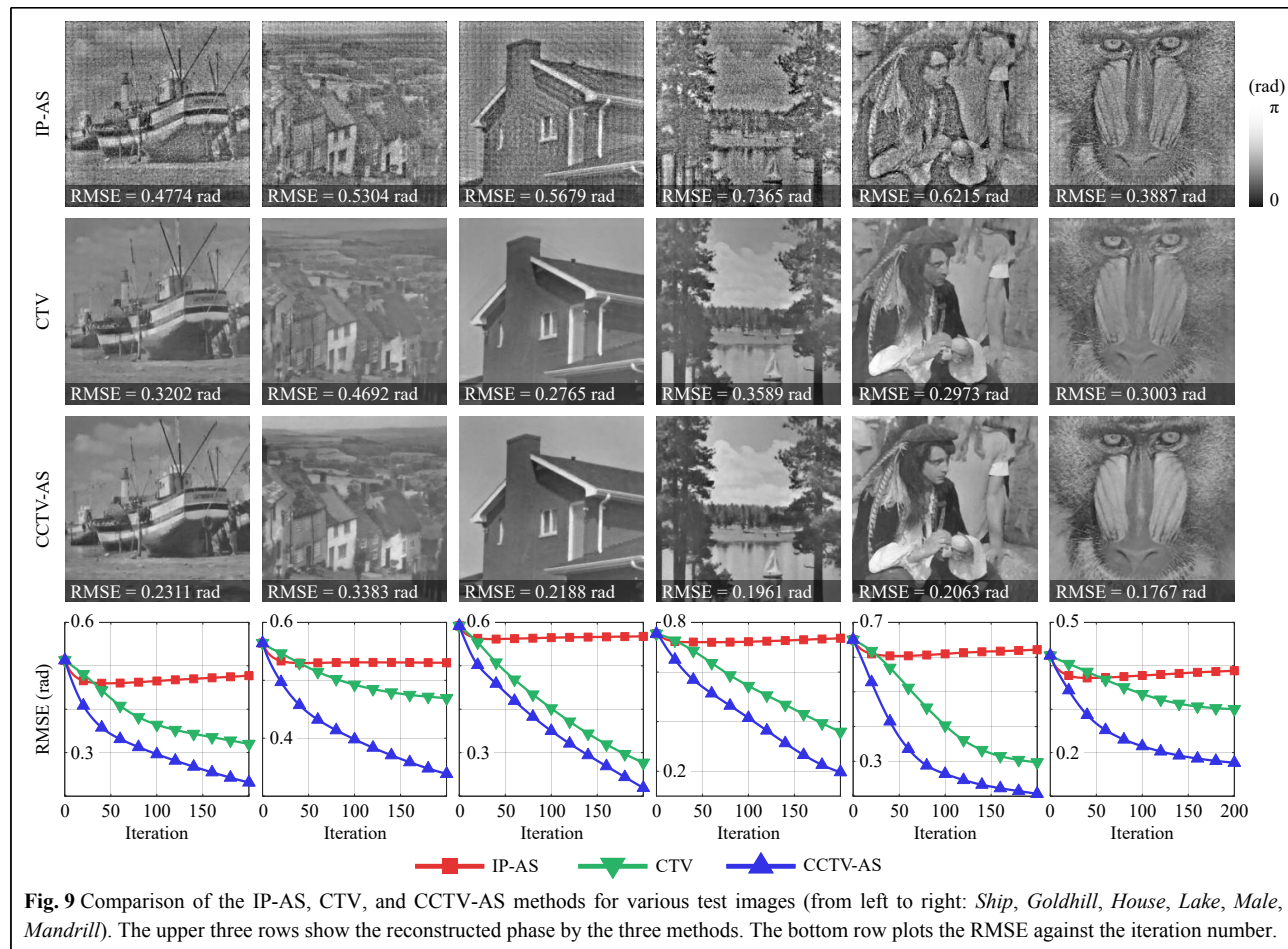


combination of sparsity priors and physical constraints. We also set $\lambda = 1 \times 10^{-2}$ as fixed throughout the simulation experiments. This implies that the selection of λ is not very sensitive to the scene content.

Nesterov acceleration for nonconvex optimization

We also empirically validated the effectiveness of Nesterov's method for the nonconvex phase retrieval

problem by comparing the APG algorithm with the non-accelerated version in both unconstrained and constrained cases, as shown in Fig. 10a, b, respectively. Nesterov's method significantly improved the convergence speed in both cases. The APG algorithm involves only an additional extrapolation step per iteration, whose time consumption is negligible compared with the gradient and proximal update steps. The empirical success of Nesterov's method can be



explained partly by the similarity between the amplitude-based fidelity function and the convex least-squares formulation¹⁰⁷.

Conclusion

We have proposed a unified compressive phase retrieval framework for in-line holography that combines the complex total variation and physical knowledge of the wavefield. The resulting CCTV model can characterize the

sparse nature of complex real-world scenes while leveraging physically tractable constraints to further improve imaging quality, as confirmed by both simulated and optical experiments. In addition, we conducted a detailed theoretical analysis from a mathematical viewpoint, which provides general guidance for algorithm parameter selection to ensure convergence, obviating the need for laborious manual tuning. We emphasize that the proposed framework is generally applicable to various optical configurations and can easily adapt to other physical constraints and sparsifying operators.

Although numerically extending the proposed algorithmic framework to coherent diffraction imaging is straightforward, retrieving complex-valued images from a single far-field diffraction pattern remains challenging. Future work will explore more advanced image priors that enable snapshot coherent diffraction imaging of complex samples¹³⁵. Another direction for future research is to achieve quantitative phase imaging of objects with a large phase shift, as only weak phase objects have been tested in this work. Comparison of the proposed method with other

existing quantitative phase imaging methods also remains to be studied in the future^{136,137}.

Acknowledgements

The authors acknowledge the National Natural Science Foundation of China (Grant No. 61827825) for financial support. The authors would also like to thank the anonymous reviewers for their constructive comments and suggestions, which improved the presentation of the paper. Part of this paper was posted as a preprint¹³⁸ before submission.

Conflict of interest

The authors declare no conflicts of interest.

Supplementary information is available for this paper at <https://doi.org/10.37188/lam.2023.006>.

Received: 07 June 2022 Revised: 01 February 2023 Accepted: 03 February 2023

Accepted article preview online: 04 February 2023

Published online: 11 March 2023

References

1. Gabor, D. A new microscopic principle. *Nature* **161**, 777-778 (1948).
2. Javidi, B. et al. Roadmap on digital holography [Invited]. *Optics Express* **29**, 35078-35118 (2021).
3. Sheridan, J. T. et al. Roadmap on holography. *Journal of Optics* **22**, 123002 (2020).
4. Liu, G. & Scott, P. D. Phase retrieval and twin-image elimination for in-line Fresnel holograms. *Journal of the Optical Society of America A* **4**, 159-165 (1987).
5. Barton, J. J. Removing multiple scattering and twin images from holographic images. *Physical Review Letters* **67**, 3106-3109 (1991).
6. Shechtman, Y. et al. Phase retrieval with application to optical imaging: a contemporary overview. *IEEE Signal Processing Magazine* **32**, 87-109 (2015).
7. Dong, J. et al. Phase retrieval: from computational imaging to machine learning: a tutorial. *IEEE Signal Processing Magazine* **40**, 45-57 (2023).
8. Almoro, P., Pedrini, G. & Osten, W. Complete wavefront reconstruction using sequential intensity measurements of a volume speckle field. *Applied Optics* **45**, 8596-8605 (2006).
9. Waller, L., Tian, L. & Barbastathis, G. Transport of intensity phase-amplitude imaging with higher order intensity derivatives. *Optics Express* **18**, 12552-12561 (2010).
10. Zuo, C. et al. Transport of intensity equation: a tutorial. *Optics and Lasers in Engineering* **135**, 106187 (2020).
11. Bao, P. et al. Phase retrieval using multiple illumination wavelengths. *Optics Letters* **33**, 309-311 (2008).
12. Bai, Y. R. et al. Ptychographic microscopy via wavelength scanning. *APL Photonics* **2**, 056101 (2017).
13. Fan, Y. et al. Single-shot isotropic quantitative phase microscopy based on color-multiplexed differential phase contrast. *APL Photonics* **4**, 121301 (2019).
14. Gao, Y. H. & Cao, L. C. Projected refractive index framework for multi-wavelength phase retrieval. *Optics Letters* **47**, 5965-5968 (2022).
15. Faulkner, H. M. L. & Rodenburg, J. M. Movable aperture lensless transmission microscopy: a novel phase retrieval algorithm. *Physical Review Letters* **93**, 023903 (2004).
16. Zhang, Z. B. et al. Invited article: mask-modulated lensless imaging with multi-angle illuminations. *APL Photonics* **3**, 060803 (2018).
17. Jiang, S. W. et al. Wide-field, high-resolution lensless on-chip microscopy via near-field blind ptychographic modulation. *Lab on a Chip* **20**, 1058-1065 (2020).
18. Zheng, G. A., Horstmeyer, R. & Yang, C. Wide-field, high-resolution Fourier ptychographic microscopy. *Nature Photonics* **7**, 739-745 (2013).
19. Tian, L. et al. Computational illumination for high-speed *in vitro* Fourier ptychographic microscopy. *Optica* **2**, 904-911 (2015).
20. Zheng, G. A. et al. Concept, implementations and applications of Fourier ptychography. *Nature Reviews Physics* **3**, 207-223 (2021).
21. Zhang, F. C., Pedrini, G. & Osten, W. Phase retrieval of arbitrary complex-valued fields through aperture-plane modulation. *Physical Review A* **75**, 043805 (2007).
22. Katkovnik, V. et al. Computational super-resolution phase retrieval from multiple phase-coded diffraction patterns: simulation study and experiments. *Optica* **4**, 786-794 (2017).
23. Wu, Y. C., Sharma, M. K. & Veeraraghavan, A. WISH: wavefront imaging sensor with high resolution. *Light: Science & Applications* **8**, 44 (2019).
24. Li, R. J. & Cao, L. C. Complex wavefront sensing based on alternative structured phase modulation. *Applied Optics* **60**, A48-A53 (2021).
25. Fienup, J. R. Reconstruction of an object from the modulus of its Fourier transform. *Optics Letters* **3**, 27-29 (1978).
26. Tian, Y. C. & Fienup, J. R. Phase retrieval with only a nonnegativity constraint. *Optics Letters* **48**, 135-138 (2023).
27. Fienup, J. R. Reconstruction of a complex-valued object from the modulus of its Fourier transform using a support constraint. *Journal of the Optical Society of America A* **4**, 118-123 (1987).
28. Marchesini, S. et al. X-ray image reconstruction from a diffraction pattern alone. *Physical Review B* **68**, 140101 (2003).
29. Abbey, B. et al. Keyhole coherent diffractive imaging. *Nature Physics* **4**, 394-398 (2008).
30. Latychevskaia, T. & Fink, H. W. Solution to the twin image problem in holography. *Physical Review Letters* **98**, 233901 (2007).
31. Zhang, K. Y. J. & Main, P. Histogram matching as a new density modification technique for phase refinement and extension of protein molecules. *Acta Crystallographica Section A: Foundations of Crystallography* **46**, 41-46 (1990).
32. Elser, V. Solution of the crystallographic phase problem by iterated projections. *Acta Crystallographica Section A: Foundations of Crystallography* **59**, 201-209 (2003).
33. Levi, A. & Stark, H. Image restoration by the method of generalized projections with application to restoration from magnitude. *Journal of the Optical Society of America A* **1**, 932-943 (1984).
34. Elser, V. Phase retrieval by iterated projections. *Journal of the Optical Society of America A* **20**, 40-55 (2003).
35. Gerchberg, R. W. & Saxton, W. O. A practical algorithm for the determination of phase from image and diffraction plane pictures. *Optik* **35**, 237-246 (1972).
36. Fienup, J. R. Phase retrieval algorithms: a comparison. *Applied Optics* **21**, 2758-2769 (1982).
37. Bauschke, H. H., Combettes, P. L. & Luke, D. R. Phase retrieval, error reduction algorithm, and Fienup variants: a view from convex optimization. *Journal of the Optical Society of America A* **19**, 1334-1345 (2002).
38. Marchesini, S. Invited article: a unified evaluation of iterative projection algorithms for phase retrieval. *Review of Scientific Instruments* **78**, 011301 (2007).
39. Latychevskaia, T. Iterative phase retrieval for digital holography: tutorial. *Journal of the Optical Society of America A* **36**, D31-D40 (2019).
40. Rong, L. et al. Twin image elimination from two in-line holograms via

- phase retrieval. *Chinese Optics Letters* **10**, 060902 (2012).
- 41. Brady, D. J. et al. Compressive holography. *Optics Express* **17**, 13040-13049 (2009).
 - 42. Rivenson, Y., Stern, A. & Javidi, B. Compressive Fresnel holography. *Journal of Display Technology* **6**, 506-509 (2010).
 - 43. Rivenson, Y., Stern, A. & Javidi, B. Overview of compressive sensing techniques applied in holography. *Applied Optics* **52**, A423-A432 (2013).
 - 44. Moravec, M. L., Romberg, J. K. & Baraniuk, R. G. Compressive phase retrieval. Proceedings of SPIE 6701, Wavelets XII. San Diego, CA, USA: SPIE, 2007, 712-722.
 - 45. Shechtman, Y., Beck, A. & Eldar, Y. C. GESPAR: Efficient phase retrieval of sparse signals. *IEEE Transactions on Signal Processing* **62**, 928-938 (2014).
 - 46. Jagannathan, K., Oymak, S. & Hassibi, B. Sparse phase retrieval: uniqueness guarantees and recovery algorithms. *IEEE Transactions on Signal Processing* **65**, 2402-2410 (2017).
 - 47. Denis, L. et al. Inline hologram reconstruction with sparsity constraints. *Optics Letters* **34**, 3475-3477 (2009).
 - 48. Wang, G. et al. Sparse phase retrieval via truncated amplitude flow. *IEEE Transactions on Signal Processing* **66**, 479-491 (2018).
 - 49. Pacheco, C. et al. Adaptive sparse reconstruction for lensless digital holography via PSF estimation and phase retrieval. *Optics Express* **30**, 33433-33448 (2022).
 - 50. Kostenko, A. et al. Phase retrieval in in-line x-ray phase contrast imaging based on total variation minimization. *Optics Express* **21**, 710-723 (2013).
 - 51. Horisaki, R. et al. Single-shot phase imaging with a coded aperture. *Optics Letters* **39**, 6466-6469 (2014).
 - 52. Horisaki, R., Egami, R. & Tanida, J. Single-shot phase imaging with randomized light (SPIRaL). *Optics Express* **24**, 3765-3773 (2016).
 - 53. Zhang, W. H. et al. Twin-image-free holography: a compressive sensing approach. *Physical Review Letters* **121**, 093902 (2018).
 - 54. Momey, F. et al. From Fienupos phase retrieval techniques to regularized inversion for in-line holography: tutorial. *Journal of the Optical Society of America A* **36**, D62-D80 (2019).
 - 55. Jolivet, F. et al. Regularized reconstruction of absorbing and phase objects from a single in-line hologram, application to fluid mechanics and micro-biology. *Optics Express* **26**, 8923-8940 (2018).
 - 56. Chang, H. B. et al. Total variation-based phase retrieval for Poisson noise removal. *SIAM Journal on Imaging Sciences* **11**, 24-55 (2018).
 - 57. Guo, C. et al. Lensfree on-chip microscopy based on dual-plane phase retrieval. *Optics Express* **27**, 35216-35229 (2019).
 - 58. Wu, J. C., Yang, F. & Cao, L. C. Resolution enhancement of long-range imaging with sparse apertures. *Optics and Lasers in Engineering* **155**, 107068 (2022).
 - 59. Gaur, C., Mohan, B. & Khare, K. Sparsity-assisted solution to the twin image problem in phase retrieval. *Journal of the Optical Society of America A* **32**, 1922-1927 (2015).
 - 60. Villanueva-Perez, P. et al. Contrast-transfer-function phase retrieval based on compressed sensing. *Optics Letters* **42**, 1133-1136 (2017).
 - 61. Galande, A. S. et al. Quantitative phase imaging of biological cells using lensless inline holographic microscopy through sparsity-assisted iterative phase retrieval algorithm. *Journal of Applied Physics* **132**, 243102 (2022).
 - 62. Rivenson, Y. et al. Sparsity-based multi-height phase recovery in holographic microscopy. *Scientific Reports* **6**, 37862 (2016).
 - 63. Loock, S. & Plonka, G. Phase retrieval for Fresnel measurements using a shearlet sparsity constraint. *Inverse Problems* **30**, 055005 (2014).
 - 64. Pein, A. et al. Using sparsity information for iterative phase retrieval in x-ray propagation imaging. *Optics Express* **24**, 8332-8343 (2016).
 - 65. Tillmann, A. M., Eldar, Y. C. & Mairal, J. DOLPHIn: dictionary learning for phase retrieval. *IEEE Transactions on Signal Processing* **64**, 6485-6500 (2016).
 - 66. Krishnan, J. P., Bioucas-Dias, J. M. & Katkovnik, V. Dictionary learning for phase retrieval from noisy diffraction patterns. *Sensors* **18**, 4006 (2018).
 - 67. Li, X. Y. et al. Dictionary-based compressive Fourier ptychography. *Optics Letters* **47**, 2314-2317 (2022).
 - 68. Heide, F. et al. ProxImaL: Efficient image optimization using proximal algorithms. *ACM Transactions on Graphics* **35**, 84 (2016).
 - 69. Katkovnik, V. & Astola, J. Phase retrieval via spatial light modulator phase modulation in 4f optical setup: numerical inverse imaging with sparse regularization for phase and amplitude. *Journal of the Optical Society of America A* **29**, 105-116 (2012).
 - 70. Metzler, C. A., Maleki, A. & Baraniuk, R. G. BM3D-PRGAMP: compressive phase retrieval based on BM3D denoising. Proceedings of 2016 IEEE International Conference on Multimedia & Expo Workshops. Seattle, WA, USA: IEEE, 2016, 2504-2508.
 - 71. Shi, B. S. et al. Constrained phase retrieval: when alternating projection meets regularization. *Journal of the Optical Society of America B* **35**, 1271-1281 (2018).
 - 72. Jin, X. Y. et al. Iterative denoising phase retrieval method for twin-image elimination in continuous-wave terahertz in-line digital holography. *Optics and Lasers in Engineering* **152**, 106986 (2022).
 - 73. Guo, C. et al. Lensfree on-chip microscopy based on single-plane phase retrieval. *Optics Express* **30**, 19855-19870 (2022).
 - 74. Sinha, A. et al. Lensless computational imaging through deep learning. *Optica* **4**, 1117-1125 (2017).
 - 75. Nguyen, T. et al. Deep learning approach for Fourier ptychography microscopy. *Optics Express* **26**, 26470-26484 (2018).
 - 76. Rivenson, Y., Wu, Y. C. & Ozcan, A. Deep learning in holography and coherent imaging. *Light: Science & Applications* **8**, 85 (2019).
 - 77. Hand, P., Leong, O. & Voroninski, V. Phase retrieval under a generative prior. Proceedings of the 32nd International Conference on Neural Information Processing Systems. Montréal, Canada: Curran Associates Inc., 2018, 9154-9164.
 - 78. Metzler, C. et al. prDeep: robust phase retrieval with a flexible deep network. Proceedings of the 35th International Conference on Machine Learning. Stockholm, Sweden: PMLR, 2018, 3501-3510.
 - 79. İlşil, Ç., Oktem, F. S. & Koç, A. Deep iterative reconstruction for phase retrieval. *Applied Optics* **58**, 5422-5431 (2019).
 - 80. Wang, Y. T., Sun, X. H. & Fleischer, J. When deep denoising meets iterative phase retrieval. Proceedings of the 37th International Conference on Machine Learning. Online, PMLR, 2020, 10007-10017.
 - 81. Shi, B. S., Li, J. Q. S. & Chang, H. B. Deep prior-based sparse representation model for diffraction imaging: A plug-and-play method. *Signal Processing* **168**, 107350 (2020).
 - 82. Wang, F. et al. Phase imaging with an untrained neural network. *Light: Science & Applications* **9**, 77 (2020).
 - 83. Bostan, E. et al. Deep phase decoder: self-calibrating phase microscopy with an untrained deep neural network. *Optica* **7**, 559-562 (2020).
 - 84. Chang, X. Y., Bi, L. H. & Zhang, J. Large-scale phase retrieval. *eLight* **1**, 4 (2021).
 - 85. Zhang, F. L. et al. Physics-based iterative projection complex neural network for phase retrieval in lensless microscopy imaging. Proceedings of 2021 IEEE/CVF Conference on Computer Vision and Pattern Recognition. Nashville, TN, USA: IEEE, 2021, 10518-10526.
 - 86. Zhang, X. Y., Wang, F. & Situ, G. H. BlindNet: an untrained learning approach toward computational imaging with model uncertainty. *Journal of Physics D: Applied Physics* **55**, 034001 (2021).

87. Yang, D. Y. et al. Coherent modulation imaging using a physics-driven neural network. *Optics Express* **30**, 35647-35662 (2022).
88. Chen, Z. J. et al. Phase recovery with deep complex-domain priors. *IEEE Signal Processing Letters* **29**, 887-891 (2022).
89. Kang, I. et al. Simultaneous spectral recovery and CMOS micro-LED holography with an untrained deep neural network. *Optica* **9**, 1149-1155 (2022).
90. Zhu, H. et al. DNF: diffractive neural field for lensless microscopic imaging. *Optics Express* **30**, 18168-18178 (2022).
91. Tian, Z. M. et al. Lensless computational imaging with a hybrid framework of holographic propagation and deep learning. *Optics Letters* **47**, 4283-4286 (2022).
92. Luo, H. X. et al. Diffraction-Net: a robust single-shot holography for multi-distance lensless imaging. *Optics Express* **30**, 41724-41740 (2022).
93. Situ, G. H. Deep holography. *Light: Advanced Manufacturing* **3**, 278-300 (2022).
94. Rudin, L. I., Osher, S. & Fatemi, E. Nonlinear total variation based noise removal algorithms. *Physica D: Nonlinear Phenomena* **60**, 259-268 (1992).
95. Chambolle, A. An algorithm for total variation minimization and applications. *Journal of Mathematical Imaging and Vision* **20**, 89-97 (2004).
96. Fabian, Z. et al. 3D phase retrieval at nano-scale via accelerated Wirtinger flow. Proceedings of the 2020 28th European Signal Processing Conference. Amsterdam, Netherlands: IEEE, 2021, 2080-2084.
97. Berdeu, A. et al. Comparative study of fully three-dimensional reconstruction algorithms for lens-free microscopy. *Applied Optics* **56**, 3939-3951 (2017).
98. Chen, M. et al. Multi-layer Born multiple-scattering model for 3D phase microscopy. *Optica* **7**, 394-403 (2020).
99. Sun, D. et al. Influence of sparse constraint functions on compressive holographic tomography. *Applied Optics* **60**, A111-A119 (2021).
100. Daloglu, M. U. et al. Low-cost and portable UV holographic microscope for high-contrast protein crystal imaging. *APL Photonics* **4**, 030804 (2019).
101. Valzania, L. et al. THz coherent lensless imaging. *Applied Optics* **58**, G256-G275 (2019).
102. Goodman, J. W. Introduction to Fourier Optics. 3rd edn. (Greenwoood Village: Roberts and Company Publishers, 2005).
103. Matakos, A., Ramani, S. & Fessler, J. A. Accelerated edge-preserving image restoration without boundary artifacts. *IEEE Transactions on Image Processing* **22**, 2019-2029 (2013).
104. Candès, E. J., Li, X. D. & Soltanolkotabi, M. Phase retrieval via Wirtinger flow: theory and algorithms. *IEEE Transactions on Information Theory* **61**, 1985-2007 (2015).
105. Sun, J., Qu, Q. & Wright, J. A geometric analysis of phase retrieval. *Foundations of Computational Mathematics* **18**, 1131-1198 (2018).
106. Isernia, T., Leone, G. & Pierri, R. Radiation pattern evaluation from near-field intensities on planes. *IEEE Transactions on Antennas and Propagation* **44**, 701 (1996).
107. Zhang, H. S. & Liang, Y. B. Reshaped Wirtinger flow for solving quadratic system of equations. Proceedings of the 30th International Conference on Neural Information Processing Systems. Barcelona, Spain: Curran Associates Inc., 2016, 2630-2638.
108. Wang, G., Giannakis, G. B. & Eldar, Y. C. Solving systems of random quadratic equations via truncated amplitude flow. *IEEE Transactions on Information Theory* **64**, 773-794 (2017).
109. Yang, C. et al. Iterative algorithms for ptychographic phase retrieval. (Berkeley, CA, USA: Lawrence Berkeley National Lab., 2011).
110. Fanjiang, A. & Strohmer, T. The numerics of phase retrieval. *Acta Numerica* **29**, 125-228 (2020).
111. Yeh, L. H. et al. Experimental robustness of Fourier ptychography phase retrieval algorithms. *Optics Express* **23**, 33214-33240 (2015).
112. Gao, Y. H. & Cao, L. C. Generalized optimization framework for pixel super-resolution imaging in digital holography. *Optics Express* **29**, 28805-28823 (2021).
113. Aghamiry, H. S., Gholami, A. & Operto, S. Complex-valued imaging with total variation regularization: an application to full-waveform inversion in visco-acoustic media. *SIAM Journal on Imaging Sciences* **14**, 58-91 (2021).
114. Zhang, Y. B. et al. Edge sparsity criterion for robust holographic autofocusing. *Optics Letters* **42**, 3824-3827 (2017).
115. Ren, Z. B., Xu, Z. M. & Lam, E. Y. Learning-based nonparametric autofocusing for digital holography. *Optica* **5**, 337-344 (2018).
116. Trusiak, M. et al. Darkfocus: numerical autofocusing in digital in-line holographic microscopy using variance of computational dark-field gradient. *Optics and Lasers in Engineering* **134**, 106195 (2020).
117. Zhang, J. L. et al. Resolution analysis in a lens-free on-chip digital holographic microscope. *IEEE Transactions on Computational Imaging* **6**, 697-710 (2020).
118. Huang, Z. Z. et al. Dual-plane coupled phase retrieval for non-prior holographic imaging. *Photonix* **3**, 3 (2022).
119. Tang, J. et al. Comparison of common-path off-axis digital holography and transport of intensity equation in quantitative phase measurement. *Optics and Lasers in Engineering* **157**, 107126 (2022).
120. Rivenson, Y. et al. PhaseStain: the digital staining of label-free quantitative phase microscopy images using deep learning. *Light: Science & Applications* **8**, 23 (2019).
121. Jiang, S. W. et al. Resolution-enhanced parallel coded ptychography for high-throughput optical imaging. *ACS Photonics* **8**, 3261-3271 (2021).
122. Onural, L. Sampling of the diffraction field. *Applied Optics* **39**, 5929-5935 (2000).
123. Kelly, D. P. et al. Resolution limits in practical digital holographic systems. *Optical Engineering* **48**, 095801 (2009).
124. Kelly, D. P. et al. Quantifying the 2.5D imaging performance of digital holographic systems. *Journal of the European Optical Society* **6**, 11034 (2011).
125. Luo, W. et al. Propagation phasor approach for holographic image reconstruction. *Scientific Reports* **6**, 22738 (2016).
126. Gao, Y. H., Yang, F. & Cao, L. C. Pixel super-resolution phase retrieval for lensless on-chip microscopy via accelerated Wirtinger flow. *Cells* **11**, 1999 (2022).
127. Kreutz-Delgado, K. The complex gradient operator and the CR-calculus. arXiv: 0906.4835 (2009).
128. Parikh, N. & Boyd, S. Proximal algorithms. *Foundations and Trends' in Optimization* **1**, 127-239 (2014).
129. Nesterov, Y. E. A method for solving the convex programming problem with convergence rate $\mathcal{O}(1/k^2)$. *Soviet Mathematics Doklady* **269**, 543-547 (1983).
130. Beck, A. & Teboulle, M. A fast iterative shrinkage-thresholding algorithm for linear inverse problems. *SIAM Journal on Imaging Sciences* **2**, 183-202 (2009).
131. Beck, A. & Teboulle, M. Fast gradient-based algorithms for constrained total variation image denoising and deblurring problems. *IEEE Transactions on Image Processing* **18**, 2419-2434 (2009).
132. Xu, R. et al. Accelerated Wirtinger flow: a fast algorithm for ptychography. arXiv: 1806.05546 (2018).
133. Schmidt, M., Le Roux, N. & Bach, F. Convergence rates of inexact

- proximal-gradient methods for convex optimization. Proceedings of the 24th International Conference on Neural Information Processing Systems. Granada, Spain: Curran Associates Inc., 2011, 1458–1466.
- 134. Gao, Y. H. & Cao, L. C. Compressive phase retrieval via constrained complex total variation regularization (CCTV). at <https://github.com/THUHololab/CCTV-phase-retrieval>.
 - 135. Ye, Q. L., Wang, L. W. & Lun, D. P. K. Towards practical single-shot phase retrieval with physics-driven deep neural network. arXiv: 2208.08604 (2022).
 - 136. Baek, Y. S. & Park, Y. K. Intensity-based holographic imaging via space-domain Kramers-Kronig relations. *Nature Photonics* **15**, 354–360 (2021).
 - 137. Zhang, J. W. et al. A review of common-path off-axis digital holography: towards high stable optical instrument manufacturing. *Light: Advanced Manufacturing* **2**, 333-349 (2021).
 - 138. Gao, Y. H. & Cao, L. C. A complex constrained total variation image denoising algorithm with application to phase retrieval. arXiv: 2109.05496 (2021).